Mechanistic evidence for tracking the seasonality of photosynthesis with solar-induced fluorescence

Troy S. Magney[a,b,1], David R. Bowling[c], Barry A. Logan[d], Katja Grossmann[e,2], Jochen Stutz[e], Peter D. Blanken[f], Sean P. Burns[f,g], Rui Cheng[a], Maria A. Garcia[c], Philipp Köhler[a], Sophia Lopez[d], Nicholas C. Parazoo[b], Brett Raczka[c], David Schimel[b], and Christian Frankenberg[a,b,1]

[a]Division of Geological and Planetary Sciences, California Institute of Technology, Pasadena, CA 91125; [b]Jet Propulsion Laboratory, California Institute of Technology, Pasadena, CA 91109; [c]School of Biological Sciences, University of Utah, Salt Lake City, UT 84112; [d]Department of Biology, Bowdoin College, Brunswick, ME 04287; [e]Department of Atmospheric and Oceanic Sciences, University of California, Los Angeles, CA 90095; [f]Department of Geography, University of Colorado, Boulder, CO 80309; and [g]Mesoscale and Microscale Meteorology Laboratory, National Center for Atmospheric Research, Boulder, CO 80301

Edited by Gregory P. Asner, Arizona State University, Tempe, AZ, and approved April 26, 2019 (received for review January 7, 2019)

Northern hemisphere evergreen forests assimilate a significant fraction of global atmospheric CO_2 but monitoring large-scale changes in gross primary production (GPP) in these systems is challenging. Recent advances in remote sensing allow the detection of solar-induced chlorophyll fluorescence (SIF) emission from vegetation, which has been empirically linked to GPP at large spatial scales. This is particularly important in evergreen forests, where traditional remote-sensing techniques and terrestrial biosphere models fail to reproduce the seasonality of GPP. Here, we examined the mechanistic relationship between SIF retrieved from a canopy spectrometer system and GPP at a winter-dormant conifer forest, which has little seasonal variation in canopy structure, needle chlorophyll content, and absorbed light. Both SIF and GPP track each other in a consistent, dynamic fashion in response to environmental conditions. SIF and GPP are well correlated (R^2 = 0.62–0.92) with an invariant slope over hourly to weekly timescales. Large seasonal variations in SIF yield capture changes in photoprotective pigments and photosystem II operating efficiency associated with winter acclimation, highlighting its unique ability to precisely track the seasonality of photosynthesis. Our results underscore the potential of new satellite-based SIF products (TROPOMI, OCO-2) as proxies for the timing and magnitude of GPP in evergreen forests at an unprecedented spatiotemporal resolution.

solar-induced fluorescence (SIF) | remote sensing | gross primary production (GPP) | photosynthesis | evergreen forest

Northern hemisphere evergreen forests represent a substantial fraction of the global carbon pool (1) and contribute significantly to the fluxes of CO_2 between the biosphere and the atmosphere (2). Evidence suggests that many high-latitude evergreen ecosystems have increased in productivity in recent years in conjunction with increasing temperature (3–5). Conversely, increasing temperature can place a strain on plant available water, thereby restricting carbon uptake and increasing ecosystem respiration and therefore net carbon loss to the atmosphere (6). Consequently, predicting the fate of evergreen systems in the context of climate change has been challenging (7). While networks of eddy covariance flux towers (8) and new satellite technologies (9, 10) observe local net CO_2 fluxes, disentangling the gross CO_2 flux components, gross primary production (GPP) (CO_2 uptake) and total ecosystem respiration (CO_2 released), is difficult (11). This is especially true for evergreen ecosystems, which undergo large seasonal shifts in light-use efficiency (LUE) (carbon gained per light absorbed) while canopy structure and green leaf/needle area remain relatively constant (12), making classical remote-sensing parameters—such as the normalized difference vegetation index (NDVI) and enhanced vegetation index (EVI)—poorly suited for detecting seasonal GPP change (13, 14). Additional challenges in vegetation remote sensing arise in high-latitude ecosystems due to pervasive cloudiness, shadow contamination, snow, and open water surfaces (15). Further, the complex terrain of high-elevation evergreen systems is generally not amenable to eddy covariance carbon flux measurements. As a result, accurately determining the timing of seasonal GPP onset and cessation in evergreen forests remains a major challenge in terrestrial biosphere models and satellite remote sensing (7, 16, 17).

Recent advances in satellite remote sensing of solar-induced chlorophyll fluorescence (SIF) may help overcome these challenges (18–22) by providing a proxy for GPP (16, 23–25). SIF represents an emission of energy emanating from chlorophyll molecules, which is a function of the activity of competing pathways for de-excitation [principally by photochemistry and nonphotochemical quenching (NPQ)] (26). Evergreen forests experience strong seasonality and endure significant physiological stress during the winter while still absorbing considerable sunlight (27). To acclimate, conifers reduce the abundance of reaction center proteins and increase their investment in photoprotective pigments (zeaxanthin and antheraxanthin) associated

Significance

Recent advances in satellite remote sensing of solar-induced fluorescence (SIF) are promising for estimating gross primary production (GPP). However, the empirical link between GPP and SIF has mostly been observed at coarse spatial and temporal scales and lacks a direct mechanistic explanation. Here, we compare high-resolution SIF with GPP and needle-scale physiology at a winter-dormant coniferous forest. Needles retained chlorophyll year-round despite cold temperatures and high light in winter; meanwhile SIF tracks GPP at hourly to weekly timescales. We show that both GPP and SIF are regulated by seasonal changes in photoprotective pigments and that SIF is directly related to needle physiology. This highlights the unique ability of SIF compared with traditional remote-sensing methods to capture GPP seasonality.

Author contributions: T.S.M., D.R.B., B.A.L., K.G., J.S., and C.F. designed research; T.S.M., D.R.B., B.A.L., K.G., J.S., P.D.B., S.P.B., M.A.G., S.L., and C.F. performed research; T.S.M., D.R.B., B.A.L., K.G., J.S., S.P.B., R.C., M.A.G., P.K., S.L., N.C.P., B.R., and C.F. analyzed data; and T.S.M., D.R.B., B.A.L., K.G., J.S., P.D.B., S.P.B., P.K., N.C.P., B.R., D.S., and C.F. wrote the paper.

The authors declare no conflict of interest.

This article is a PNAS Direct Submission.

Data deposition: Our data are provided as time series with all of the relevant variables presented in the paper. The data can be found at https://data.caltech.edu/records/1231. The data are saved as a .csv file.

[1]To whom correspondence may be addressed. Email: tmagney@caltech.edu or cfranken@caltech.edu.

[2]Present address: Institute of Environmental Physics, University of Heidelberg, D-69120 Heidelberg, Germany.

This article contains supporting information online at www.pnas.org/lookup/suppl/doi:10.1073/pnas.1900278116/-/DCSupplemental.

Published online May 28, 2019.

with NPQ (28–30). Consequently, fluorescence is strongly inhibited. Some of the low level of residual fluorescence in winter-acclimated needles may be associated with photosystem I (PSI), but a small dynamic component may indicate the presence of some photosystem II (PSII) activity. However, it is unclear how this process manifests at scales observable via remote sensing.

A growing body of evidence suggests that the relationship between GPP and SIF becomes more linear over increasing spatial (31–34) and temporal (35–37) extents. A key driver of both SIF and GPP is absorbed photosynthetically active radiation (APAR) by chlorophyll (38, 39). Thus, some research suggests that SIF is primarily responding to changes in APAR—a quantity related to incident light and green leaf area—rather than actual changes in the efficiency of photosynthesis, which may be the case in deciduous forests and cropping systems (39–41). In fact, currently established parameterizations of fluorescence yields predict potential reductions in the fluorescence yields to only about 50% of their maximum (42). This should still result in substantial SIF values in cold environments when a de facto shutdown of photosynthesis occurs coincident with little change in APAR. Seasonally snow-covered evergreen systems at midlatitudes and high altitude (cold but high light in winter) provide an ideal case study for examining the relationship between SIF and GPP independent of seasonal changes in chlorophyll or APAR. We investigated this at a subalpine conifer forest (codominated by *Pinus contorta*, *Picea engelmannii*, and *Abies lasiocarpa*) at Niwot Ridge, CO. We measured SIF and NDVI continuously from June 2017 to June 2018 with a spectrometer system (43) mounted on top of an eddy covariance flux tower. Spectroscopic data were compared with APAR, meteorology, GPP, and approximately monthly characterizations of needle pigment composition and quantum efficiencies measured via active pulse-amplitude modulated (PAM) fluorimetry.

Results

Seasonal and Diurnal Dynamics of Canopy Photosynthesis and SIF. Flux tower observations indicated full cessation of CO_2 uptake at Niwot Ridge during the winter (Fig. 1*B*), with a rapid resumption of activity in April–May, and a slower decrease of activity in fall—in agreement with (44, 45). During the same time period, we observed no significant seasonal change in APAR, NDVI, or needle chlorophyll concentration, as was expected (Fig. 1 *C* and *D*). The timing and magnitude of changes in GPP during the fall and spring transition periods closely corresponded with those in SIF (Fig. 1*B*), coincident with changes in dark-acclimated xanthophyll cycle conversion state and the maximum quantum efficiency of photosystem II (F_v/F_m, Fig. 1*D*). The retention of zeaxanthin (Z) and antheraxanthin (A) in dark-acclimated foliage in winter (i.e., a high xanthophyll cycle conversion state) is associated with sustained photoprotection (28), which manifests as decreases in the maximum quantum efficiency of photosystem II when conditions are unsuitable for photosynthesis (46). The seasonal trends in needle-scale parameters confirm findings from a previous study at Niwot Ridge (27), but also provide insight into the timing of changes in leaf physiology and indicate that needles experience significant physiological stress in the winter. The 5-d running means of SIF tracked GPP closely during the growing season (Fig. 1*B*), coincident with changes in environmental conditions and relative SIF [which is normalized by incoming near-infrared (NIR) reflected radiance to account for structural and bidirectional reflectance effects of the signal (47)] (*SI Appendix*, Fig. S1). SIF showed a nearly fourfold decrease during the transition from summer to winter—which is much larger than expected using current SIF modeling paradigms (42). The residuals (daily averages) of the 5-d running means showed that SIF and GPP are significantly correlated (*SI Appendix*, Fig. S2), suggesting that SIF tracks not only the seasonal variation of GPP, but also day-to-day changes driven largely by incoming light, while NDVI was constant throughout the season (Fig. 1*C*). There was also a close correspondence between tower-based SIF (at the time of satellite overpass) and satellite-based SIF from TROPOMI (22) and OCO-2 (48) (target), the former of which was able to retrieve satellite SIF at a subweekly resolution and has a near 1:1 slope compared with tower-derived SIF (*SI Appendix*, Fig. S3). The correspondence between tower and satellite SIF is particularly encouraging given the relatively large single-footprint size of TROPOMI (3.5 × 7 km at nadir) and OCO-2 (1.3 × 2.25 km; *SI Appendix*, Fig. S4).

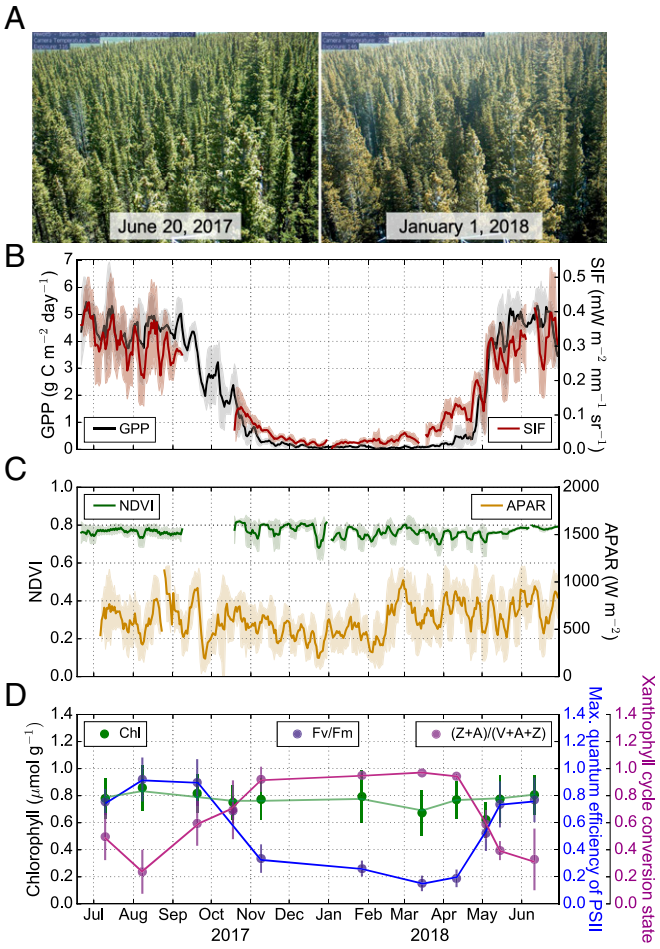

Fig. 1. Seasonal dynamics of GPP, far-red SIF, NDVI, APAR, needle pigments, and fluorescence at Niwot Ridge, CO. (*A*) Phenocam (webcam) images of the canopy where the data were collected during different seasons. (*B*) Five-day running means of cumulative daily GPP (black) and true daily average SIF (dark red). (*C*) Five-day running means of NDVI (green) and APAR (gold). Shaded regions in *B* and *C* indicate 1 SEM. (*D*) Chlorophyll a + b concentration relative to dry mass (green), maximum quantum efficiency (F_v/F_m) measured with a fluorimeter (blue), and dark-adapted xanthophyll cycle conversion state (purple) ([Zeaxanthin + Antheraxanthin]/[Violaxanthin + Antheraxanthin + Zeaxanthin]) sampled at monthly intervals. All needleleaf measurements represent the mean and 1 SE of both Engelmann spruce and lodgepole pine samples during each 2- to 3-d sampling period.

Seasonal averages of hourly data are shown to highlight the dynamic nature of GPP, light-use efficiency (GPP/APAR), SIF, SIF yield (SIF/APAR), and relative SIF (SIF/NIR reflected radiance) across the seasons (Fig. 2). In deciduous forests, there is almost no APAR or chlorophyll in the winter; but in this case, only about a 30% decrease in APAR was observed on sunny days in the winter, with no significant change in needle chlorophyll concentration (Fig. 2*F*). Meanwhile, a near complete suppression of photosynthetic activity during the winter resulted in nominal (~0) GPP and very little SIF (Fig. 2 *A* and *B* and *SI Appendix*, Fig. S5). Additionally, SIF yield, LUE, and relative SIF were significantly reduced during the summer-to-winter transition, with a similar diurnal pattern (Fig. 2 *C*–*E*). This suggests that most of the absorbed light in winter and spring was being dissipated as heat via NPQ mechanisms, largely reducing fluorescence and contributing

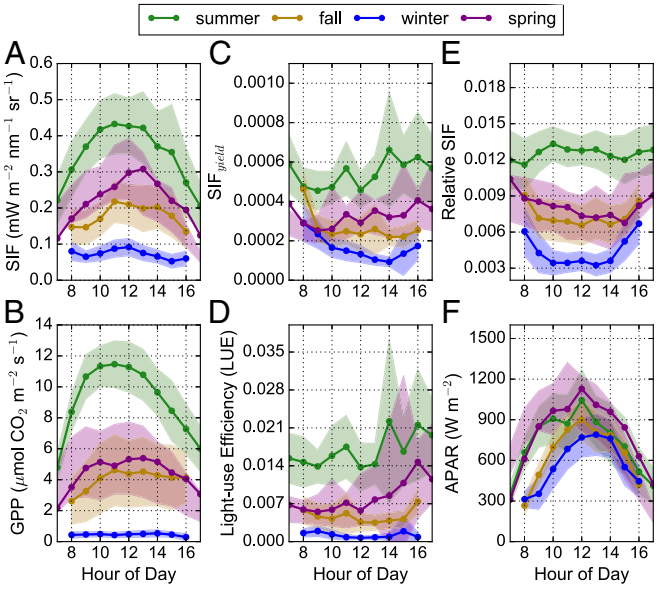

Fig. 2. (*A*–*F*) Seasonal hourly averages of (*A*) far-red SIF; (*B*) GPP; (*C*) far-red SIF yield (SIF/APAR); (*D*) LUE (GPP/APAR); (*E*) relative far-red SIF (SIF/reflected radiance in the NIR retrieval window); and (*F*) APAR. Summer data are from June 21, 2017 to August 30, 2017 and from June 1, 2018 to June 29, 2018. Fall data are from September 1, 2017 to November 15, 2017. Winter data are from November 15, 2017 to March 31, 2018. Spring data are from April 1, 2018 to May 23, 2018. Shaded regions represent 1 SE of the hourly mean. Green, summer; gold, fall; blue, winter; and purple, spring.

to the shutdown of photosynthesis. However, there was still the potential for a small amount of electron transport happening within needles, albeit at a much-reduced level, as evidenced by the F_v/F_m measurements (Fig. 1*D*). The small residual SIF emissions in winter (while GPP approaches zero) may indicate electron transport to maintain a transmembrane ΔpH needed to sustain NPQ (29). Further, the slight increase in SIF preceding GPP in the spring of 2018 could be due to photorespiratory recycling of CO_2 before stomatal opening because water transport was still blocked by frozen boles early in the spring (27). Future research is needed at both needle and canopy scales to fully understand the slightly earlier increase in fluorescence compared with GPP in evergreen coniferous ecosystems.

SIF Tracks Photosynthesis Across All Seasons and at Different Timescales. Scatterplots for hourly, daily, and weekly aggregated data shown in Figs. 1 and 2 are provided in Fig. 3. Here, we show that SIF corresponded more closely to changes in GPP than APAR at hourly ($R^2 = 0.62$ vs. $R^2 = 0.37$), daily ($R^2 = 0.78$ vs. $R^2 = 0.29$), and weekly ($R^2 = 0.92$ vs. $R^2 = 0.33$) timescales, clearly underlining that most variation was due to changes in fluorescence and photosynthetic efficiencies (Figs. 1 and 4). The stronger correlation between SIF and GPP was largely driven by more dramatic changes in the seasonality of SIF compared with APAR—i.e., photosynthesis approached zero, but absorbed light remained relatively high. Notably, the strength (R^2) of these relationships improved when the averaging period increased, but there was little difference in the slope and intercept of the GPP vs. SIF relationships at increasing timescales (Fig. 3).

Typically, the dynamic range of PSII yields at the leaf scale (under NPQ changes) is much larger than that of the SIF yield (34, 42); however, at the canopy scale, we observe a substantial reduction in SIF yield (decrease of ∼80%) in the winter due to sustained NPQ and deactivation of photosystems. Such dynamic changes in PSII yield and F_v/F_m have been shown in winter measurements of PAM fluorescence in a similar ecosystem located in Hyytiälä, Finland, which also suggests substantial suppression of photochemistry in PSII (49). We hypothesize that either the impact of sustained NPQ on SIF yields is currently underestimated or the canopy aggregation of SIF and GPP over all sunlit and shaded leaves represents a substantially more complex scenario than that in leaf-scale studies. Thus, temporal and spatial averaging of SIF data could provide credence for the consistently strong and positive relationships between SIF and GPP observed at longer (often monthly) timescales (31). Further, APAR was not associated with changes in GPP at our site as strongly as in some agricultural systems (39) (*SI Appendix*, Fig. S6). While all of the relationships shown in the main text used tower-based far-red SIF data (consistent with satellites), we also observed a close correspondence between red SIF and GPP, with no discernable difference between red and far-red SIF for tracking GPP (*SI Appendix*, Fig. S6: hourly $R^2 = 0.50$; daily $R^2 = 0.67$; and weekly $R^2 = 0.87$). We expect that red SIF will increase when chlorophyll concentration decreases (50, 51), but since no change in chlorophyll was observed, red SIF tracks far-red SIF closely (*SI Appendix*, Fig. S2). Taken together, we conclude that high-frequency daily satellite overpasses measuring red and far-red SIF (i.e., TROPOMI) will be adequate to characterize the seasonality of photosynthesis and that the SIF/GPP relationship can be extrapolated across varying timescales in a reproducible fashion. However, due to the rapid onset and cessation of photosynthesis in this forest, current satellite SIF products averaged at a monthly time resolution are not yet adequate to capture the phenological transition that influences GPP in this system (48).

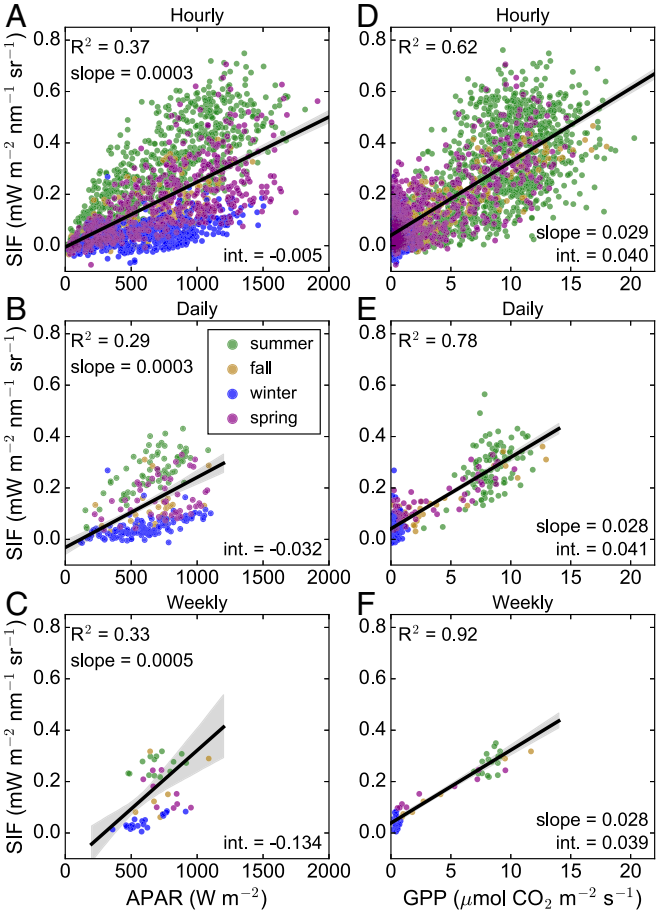

Fig. 3. (*A*–*F*) Scatterplots of (*A*–*C*) far-red SIF against APAR and (*D*–*F*) GPP binned at hourly (*A* and *D*), daily (*B* and *E*), and weekly (*C* and *F*) time intervals. Points are colored by season, dictated by onset and suppression of photosynthesis. Shaded regions indicate a 95% confidence interval around the line of best fit. We report the coefficient of determination (R^2), slope, and intercept of each line of best fit. All relationships are statistically significant at $P < 0.05$.

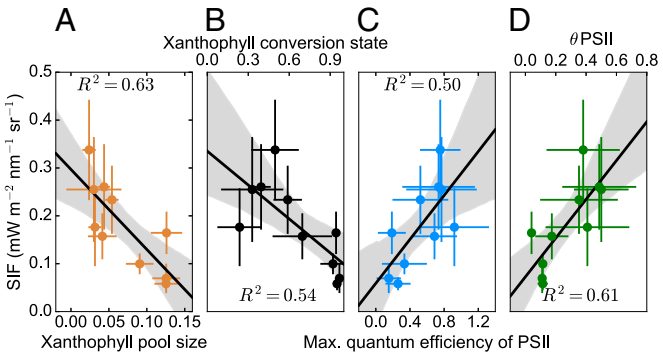

Fig. 4. Correlation plots of weekly average far-red SIF against needle measurements of foliar pigment composition and PAM fluorescence. (*A*) Total xanthophyll cycle pigment pool (V+A+Z μmol·g^{-1}). (*B*) Sustained retention of zeaxanthin and antheraxanthin after dark adaptation represented by the xanthophyll cycle conversion state ([Z+A]/[V+A+Z]). (*C*) Maximum quantum efficiency in the dark (F_v/F_m) measured by a fluorimeter. (*D*) Photosystem II operating efficiency (θPSII) at a photosynthetically active radiation (PAR) level of 500 μmol·m^{-2}·s^{-1}, derived during a light response curve. Shaded regions indicate a 95% confidence interval around the line of best fit. All relationships are statistically significant at $P < 0.05$.

Ultimately, the near-daily return interval of TROPOMI will provide a great improvement in our ability to track dynamics of photosynthesis across a wide range of ecosystems (22).

SIF Responds to Changes in Needle Physiology. Measurements of xanthophyll cycle conversion state and the quantum efficiency of photosystem II from active PAM fluorescence exhibited statistically significant relationships with weekly averages of tower-based SIF during periods of in situ sampling (Fig. 4). This confirms that the strong seasonality of GPP in this subalpine evergreen forest is modulated by changes in photosynthetic efficiency and the acclimation of photoprotective pigments in needles across two of the dominant species (*P. contorta* and *P. engelmannii*) at Niwot Ridge (27). The total xanthophyll cycle pool size (Fig. 4*A*) and retention of zeaxanthin and antheraxanthin (Figs. 1*D* and 4*B*) are representative of sustained winter photoprotection in the light-harvesting complexes (29). Our data suggest that these pools can change over the course of 2 wk in the spring (Fig. 1*D*) and that these changes coincide with increases in SIF.

It is important to note that while we draw linkages between decreasing photosynthesis, decreasing SIF, and increasing xanthophyll cycle activity, there are many other coinciding potential drivers of ecosystem productivity. At Niwot Ridge, the spring onset of photosynthesis is associated with increasing temperature, hydraulic system recovery, and an increase in carboxylation capacity (27, 52, 53). We expect not only that winter acclimation corresponds to changes in the xanthophyll cycle, but also that a variety of carotenoids, such as lutein and beta-carotene, may play a photoprotective role during the transition seasons and winter (30, 54). A continued long-term dataset of tower-based SIF and needle physiology measurements at Niwot Ridge will improve our ability to understand how SIF might respond to different controls on ecosystem carbon uptake including temperature, water availability, and evaporative demand.

Discussion

In this winter-dormant confiner forest, remotely sensed SIF reflects dynamic changes in photosynthesis at the needle (Fig. 4) and canopy scales (Figs. 1–3)—in stark contrast with traditional vegetation indexes (NDVI), which remain relatively insensitive to seasonal changes in evergreen photosynthesis. In this forest, xanthophyll cycle pigments play a significant role during winter acclimation of photosynthesis. In northern hemisphere evergreen forests, an increase in xanthophyll cycle pigments during winter is often accompanied by a decrease in chlorophyll concentration (55–57); however, we observed little seasonal change in chlorophyll concentration—coincident with previous reports at Niwot Ridge (27). An alternative measure of seasonal acclimation of leaf pigment composition is the chlorophyll:carotenoid index (CCI)—which can be detected by satellites such as MODIS—and tends to track changes in xanthophyll cycle pigments associated with winter acclimation (58). While CCI is an especially promising proxy of photosynthetic dynamics in evergreen forests, SIF has an advantage in that it is not directly impacted by fine-scale surface heterogeneity, which can bias reflectance-based indexes that are also sensitive to nonphotosynthesizing landscape features within a pixel (soil background, standing water, etc.). Additionally, SIF retrievals are less affected by clouds (59) and are not prone to saturation when leaf area is high (*SI Appendix*, Fig. S7). We report strong, statistically significant relationships between SIF and GPP at hourly, daily, and weekly timescales under both clear and diffuse sky conditions (*SI Appendix*, Fig. S7); however, it is worth noting that the slope of the relationship is lower under diffuse sky conditions, potentially because GPP can remain high even under cloudy conditions in this evergreen forest (60), and when all data are pooled together it weakens the relationship slightly (Fig. 3). The choice of a remotely sensed GPP proxy must be weighed against the available spatial and temporal resolution of the data product. Most satellite SIF data are sparse (long revisit time) and often come at a coarser spatial resolution than satellite reflectance products. OCO-2 "target mode" data provided only five observations during our study period. TROPOMI, on the other hand, will provide an order of magnitude increase in revisit frequency at high spatial resolution and retrieval precision (22), enabling a much more finely resolved time series of SIF data (22) (*SI Appendix*, Fig. S3) and improved assessment of longer-term records from GOME-2.

Previous research has highlighted the importance of understanding the nonlinear relationships between photosynthesis, fluorescence, and NPQ and how they manifest at increasing scales before interpreting SIF from space (26, 34, 42). However, our results suggest that satellite SIF from TROPOMI might be sufficient to track dynamics in photosynthesis in evergreen systems, albeit at a coarser spatial resolution (3.5 × 7 km at nadir) than that observed from tower-based observations. This is particularly relevant as state-of-the-art global terrestrial biosphere models fail to capture the seasonality of GPP in evergreen systems, often predicting an early spring uptake of CO_2 (7, 16). A potential explanation could be that global model predictions of GPP are overly sensitive to air temperature, which increases above freezing before GPP onset at Niwot Ridge (*SI Appendix*, Fig. S1). Some site-specific models have been able to circumvent these issues by providing a more detailed analysis of the timing and magnitude of GPP (45, 61, 62). To improve measuring and modeling of GPP seasonality, there is a growing network of flux towers (8) in evergreen systems that are capable of hosting tower-mounted spectrometers which could be used to further test the potential and limitations of SIF and reflectance indexes in monitoring ecosystem photosynthesis. The present study provides strong evidence for the ability of SIF to capture changes in photosynthetic capacity directly at a range of temporal scales. While greenness indexes and global models have failed to represent the magnitude and timing of GPP in winter-dormant coniferous forests, we have shown that SIF is a critical asset for improved monitoring of carbon cycle dynamics in evergreen forests. Given that higher latitudes experience amplified warming, such observations will be crucial to understand changes in carbon cycling of evergreens in the context of climate change.

Materials and Methods

Study Location. This study was conducted at a subalpine conifer forest in Colorado [the Niwot Ridge AmeriFlux Core Site US-NR1 (63), 40.03°N, 105.55°W, 3050 m elevation], over the period from June 21, 2017 to June 29, 2018. The forest is composed of three dominant evergreen needleleaf species: lodgepole pine (*P. contorta* Douglas ex Loudon), Engelmann spruce (*P. engelmannii* Parry ex Engelm.), and subalpine fir [*A. lasiocarpa* (Hook.) Nutt.]. The climate at this forest includes cold winters with a persistent snowpack from October/November to May/June. Extensive site details are available in

earlier publications (27, 60, 64). An image of the US-NR1 flux tower and PhotoSpec telescope unit is provided in *SI Appendix*, Fig. S8.

Tower-Based Solar-Induced Chlorophyll Fluorescence. Data from a scanning spectrometer (PhotoSpec) atop the 26-m tall tower were used for the canopy-scale analysis (43). Data gaps were the result of power loss to our PhotoSpec system from September 7, 2017 to October 19, 2017. The detection of SIF is based on measuring the change in the optical density of a well-known narrow spectral feature in the presence of a fluorescence signal, a solar Fraunhofer line (65–67). The instrument setup is described in detail in Grossmann et al. (43).

The PhotoSpec instrument consists of a 2D scanning telescope unit which can be pointed to any location on a canopy at user-selectable azimuth and elevation angles. Light reaching the telescope is distributed into three thermally stabilized commercial spectrometers via optical fiber bundles. These spectrometers cover wavelength ranges at high spectral resolution to retrieve SIF in the red and far-red wavelength range, as well as at moderate resolution to retrieve vegetation indices such as the NDVI. Far-red and red SIF are retrieved in the 745- to 758-nm and 680- to 686-nm wavelength windows, respectively (43). The telescope unit also includes a commercial photosynthetically active radiation (PAR) sensor (LI-COR LI-190R). A typical measurement sequence in the field started with the measurement of a solar reference spectrum using an upward-looking opal glass diffuser, followed by a scan from nadir to the horizon in 0.7° steps at two different azimuth directions, with a time resolution of ∼20 s per measurement (integration time). Diffuser spectra are recorded approximately every 3 min throughout the scanning routine. The PhotoSpec has a 0.7° field of view (FOV), resulting in an ∼20-cm diameter footprint (at nadir) on the top of the canopy. A conservative filter was applied to the SIF retrievals to ensure we were measuring data from vegetation and that measurements were not taken at unreasonably low solar or viewing zenith angles, which result in high retrieval errors. We filtered SIF data to include measurements when the solar zenith angle was less than 90°, the viewing zenith angle was less than 30°, and NDVI was greater than 0.6. The return interval for a complete scan was around 20 min, but we averaged data from all scans on an hourly time resolution to match the temporal resolution of flux tower data.

Needle Physiology. To determine seasonality of photosynthetic performance at the needle scale, physiological measurements (pigment extraction and PAM fluorescence) were performed on sun-exposed foliage from two canopy-access towers near the main flux tower and in the laboratory on branches collected from those trees, every 4–8 wk over the annual cycle. Samples came from pine and spruce trees that were in the field of view of the spectrometer. Due to canopy structure, a limited number of trees were accessible from the towers, preventing more extensive replication. This also limited sampling to *P. contorta* ad *P. engelmannii* needles. Two branches were measured/sampled from each tree during each visit ($n = 6$ branches on three trees for pine, and $n = 4$ branches on two trees for spruce, in the upper canopy at 10–12 m height above ground). We pooled species together to better match the FOV of tower- and satellite-based SIF retrievals; however, we note that no significant difference was observed between the two species at any time during the season.

Needle-Scale Chlorophyll Fluorescence. Chlorophyll fluorescence was measured on pine and spruce trees using PAM fluorimetry from a portable photosynthesis system (LI-6800F; LI-COR) equipped with the standard broadleaf chamber and control of temperature, humidity, and incident light. Two types of measurements were made, the PSII operating efficiency in the light (θPSII at 500 PAR) and the maximum quantum efficiency of PSII photochemistry (F_v/F_m on dark-acclimated tissues). Nomenclature is consistent with the review of Baker (68), except that we refer to $F_{q'}/F_{m'}$ as θPSII. To measure F_v/F_m, the distal 10–15 cm of branches were cut, wrapped in aluminum foil with a moistened paper towel, and transported to the laboratory for several hours of dark acclimation. Measurements were performed using the LI-COR 6800, after which needles were immediately flash-frozen in liquid N_2 for leaf pigment analysis.

Measurements of θPSII were made from the canopy access towers as follows. For *P. contorta*, one to two fascicles were inserted into the chamber while attached to the branch. *P. engelmannii* branch/needle geometry prevented measurements with this chamber on intact branches, so 8–10 needles were detached from the branch and affixed to adhesive tape before placing in the leaf chamber. We did not control for the orientation of the needles in the chamber (adaxial vs. abaxial). Before a measurement, ambient air temperature and light level were measured, and leaf temperature and incident light in the leaf chamber were set to match air temperature and 40% relative humidity. This was repeated for incident PAR at a light intensity of 500 μmol photons·m^{-2}·s^{-1} to determine θPSII during illumination.

Needle Chlorophyll and Carotenoid Composition. Needle pigment composition was measured to evaluate seasonal acclimation associated with the decrease in photosynthesis due to winter acclimation. Following the measurements of F_v/F_m adjacent foliage was collected and immediately flash-frozen in liquid nitrogen (LN_2) for leaf pigment analysis. Needles were stored frozen in LN_2, dry ice, or a −80 °C freezer until analysis. Pigments were extracted in acetone and analyzed by HPLC as described in Bowling et al. (27). Needle pigment contents are expressed as moles per unit fresh mass and as molar ratios (i.e., [Z + A]/[V + A + Z]). Pigments from both species during each measurement campaign were averaged, and variation was reported as 1 SD.

Meteorological Parameters and Carbon Fluxes. Weather and environmental parameters were monitored to assess their influence on forest carbon cycling. These included a wide variety of AmeriFlux Core Site observations, and the vertical exchange of CO_2, including storage, was measured at a height of 21.5 m by eddy covariance using a sonic anemometer (model CSAT3; Campbell Scientific) coupled with a closed-path infrared gas analyzer (model LI-6262; LI-COR Biosciences)—details are available in Burns et al. (60). The fluxes of GPP and ecosystem respiration were partitioned from net ecosystem exchange using air temperature following the method of Reichstein et al. (11) via the R package REddyProc (69).

The fraction of PAR absorbed by the vegetation canopy (fPAR) was computed using arrays of upward- and downward-oriented PAR sensors above and below the canopy. Full-spectrum quantum sensors (SQ-500-SS; Apogee Instruments) were new and factory-calibrated together just before installation. Above-canopy sensors (one up and one down) were mounted on the main flux tower, and below-canopy sensors (six up and six down) were mounted at 2 m height above ground via the canopy-access towers. The fPAR was calculated for each pair of below-canopy relative to above-canopy sensors, and these were averaged over daylight hours for each day to produce the seasonal pattern of APAR ($fPAR_{canopy} \times PAR_{top\ of\ canopy}$). Additionally, we tested the ability of our SIF retrievals to track GPP under clear and diffuse sky conditions using a threshold (0.5, top-of-canopy/top-of-atmosphere shortwave radiation) similar to that used in (39, 70).

Satellite Data. OCO-2 target mode observations at Niwot Ridge started in April 2017 and we used the official SIF products v8. Target collections consist of repeating backward and forward scans as the instrument flies overhead, with eight independent across-track measurements along a 10-km-wide swath and a nominal OCO-2 footprint of 1.3 km × 2.25 km. Targets are typically centered on TCCON stations for calibration of XCO_2 but centered here on the eddy covariance tower for analysis against PhotoSpec. Five targets were collected (*SI Appendix*, Fig. S3) during our sampling period and one was discarded (in June) due to excessive cloud cover. Only scenes identified as evergreen needleleaf forest were retained. Otherwise, data are quality controlled following Sun et al. (48). TROPOMI satellite data were processed according to Köhler et al. (22).

Data Availability. The datasets generated and/or analyzed for the current study are available at a data repository hosted at the California Institute of Technology (https://data.caltech.edu/records/1231). The doi associated with this dataset is 10.22002/D1.1231 (71).

ACKNOWLEDGMENTS. We thank Dave Eriksson and the support staff at University of Colorado Mountain Research Station for help during field deployment of the canopy access towers and PhotoSpec; Prof. John Lin for enthusiastic support of this research and many helpful discussions; Dr. Greg Ostermann for setting up OCO-2 target selections; Dr. Andrew Richardson for making the PhenoCam data (Fig. 1*A*) available; and Apogee Instruments for donating quantum sensors. This research was funded by a NASA Postdoctoral Program Fellowship (to T.S.M.); a Langbein Summer Research Fellowship (to S.L.); California Institute of Technology startup funds (to C.F.); the Keck Institute for Space Studies; and NASA Awards NNX16AP33G (to D.R.B.), NNX17AE14G (to C.F.), and NNX15AH95G (to C.F.). Funding for the AmeriFlux core site data (US-NR1/Niwot Ridge; principal investigator, P.D.B.) was supported by the US Department of Energy Office of Science through the AmeriFlux Management Project at Lawrence Berkeley National Laboratory under Award 7094866. The National Center for Atmospheric Research is sponsored by the NSF. These data were produced by the OCO-2 project at the Jet Propulsion Laboratory, California Institute of Technology, and obtained from the OCO-2 data archive maintained at the NASA Goddard Earth Science Data and Information Services Center. This research was carried out, in part, at the Jet Propulsion Laboratory, California Institute of Technology, under a contract with NASA. Government sponsorship acknowledged.

1. M. Thurner *et al*., Carbon stock and density of northern boreal and temperate forests. *Glob. Ecol. Biogeogr.* **23**, 297–310 (2014).
2. C. Beer *et al*., Terrestrial gross carbon dioxide uptake: Global distribution and covariation with climate. *Science* **329**, 834–839 (2010).
3. R. B. Myneni, C. D. Keeling, C. J. Tucker, G. Asrar, R. R. Nemani, Increased plant growth in the northern high latitudes from 1981 to 1991. *Nature* **386**, 698–702 (1997).
4. J. T. Randerson, C. B. Field, I. Y. Fung, P. P. Tans, Increases in early season ecosystem uptake explain recent changes in the seasonal cycle of atmospheric CO2 at high northern latitudes. *Geophys. Res. Lett.* **26**, 2765–2768 (1999).
5. M. Forkel *et al*., Enhanced seasonal CO2 exchange caused by amplified plant productivity in northern ecosystems. *Science* **351**, 696–699 (2016).
6. M. W. Trahan, B. A. Schubert, Temperature-induced water stress in high-latitude forests in response to natural and anthropogenic warming. *Glob. Chang. Biol.* **22**, 782–791 (2016).
7. A. Anav *et al*., Spatiotemporal patterns of terrestrial gross primary production: A review. *Rev. Geophys.* **53**, 785–818 (2015).
8. D. D. Baldocchi, 'Breathing' of the terrestrial biosphere: Lessons learned from a global network of carbon dioxide flux measurement systems. *Aust. J. Bot.* **56**, 1–26 (2008).
9. A. Eldering *et al*., The orbiting carbon observatory-2 early science investigations of regional carbon dioxide fluxes. *Science* **358**, eaam5745 (2017).
10. T. Yokota *et al*., Global concentrations of CO2 and CH4 retrieved from GOSAT: First preliminary results. *SOLA* **5**, 160–163 (2009).
11. M. Reichstein *et al*., On the separation of net ecosystem exchange into assimilation and ecosystem respiration: Review and improved algorithm. *Glob. Chang. Biol.* **11**, 1424–1439 (2005).
12. K. R. Springer, R. Wang, J. A. Gamon, Parallel seasonal patterns of photosynthesis, fluorescence, and reflectance indices in boreal trees. *Remote Sens.* **9**, 1–18 (2017).
13. D. A. Sims *et al*., On the use of MODIS EVI to assess gross primary productivity of North American ecosystems. *J. Geophys. Res. Biogeosci.* **111**, 1–16 (2006).
14. M. F. Garbulsky *et al*., Patterns and controls of the variability of radiation use efficiency and primary productivity across terrestrial ecosystems. *Glob. Ecol. Biogeogr.* **19**, 253–267 (2010).
15. J. A. Gamon, K. F. Huemmrich, R. S. Stone, C. E. Tweedie, Spatial and temporal variation in primary productivity (NDVI) of coastal Alaskan tundra: Decreased vegetation growth following earlier snowmelt. *Remote Sens. Environ.* **129**, 144–153 (2013).
16. N. C. Parazoo *et al*., Spring photosynthetic onset and net CO2 uptake in Alaska triggered by landscape thawing. *Glob. Chang. Biol.* **24**, 3416–3435 (2018).
17. D. P. Turner *et al*., Site-level evaluation of satellite-based global terrestrial gross primary production and net primary production monitoring. *Glob. Chang. Biol.* **11**, 666–684 (2005).
18. C. Frankenberg *et al*., New global observations of the terrestrial carbon cycle from GOSAT: Patterns of plant fluorescence with gross primary productivity. *Geophys. Res. Lett.* **38**, L17706 (2011).
19. J. Joiner, Y. Yoshida, A. P. Vasilkov, L. A. Corp, E. M. Middleton, First observations of global and seasonal terrestrial chlorophyll fluorescence from space. *Biogeosciences* **8**, 637–651 (2011).
20. L. Guanter *et al*., Global and time-resolved monitoring of crop photosynthesis with chlorophyll fluorescence. *Proc. Natl. Acad. Sci. U.S.A.* **111**, E1327–E1333 (2014).
21. Sun Y *et al*., OCO-2 advances photosynthesis observation from space via solar-induced chlorophyll fluorescence. *Science* **358**, eaam5747 (2017).
22. P. Köhler *et al*., Global retrievals of solar induced chlorophyll fluorescence with TROPOMI: First results and inter-sensor comparison to OCO-2. *Geophys. Res. Lett.* **45**, 456–463 (2018).
23. S. Walther *et al*., Satellite chlorophyll fluorescence measurements reveal large-scale decoupling of photosynthesis and greenness dynamics in boreal evergreen forests. *Glob. Chang. Biol.* **22**, 2979–2996 (2016).
24. S. J. Jeong *et al*., Application of satellite solar-induced chlorophyll fluorescence to understanding large-scale variations in vegetation phenology and function over northern high latitude forests. *Remote Sens. Environ.* **190**, 178–187 (2017).
25. L. M. Zuromski *et al*., Solar-induced fluorescence detects interannual variation in gross primary production of coniferous forests in the Western United States. *Geophys. Res. Lett.* **45**, 7184–7193 (2018).
26. A. Porcar-Castell *et al*., Linking chlorophyll a fluorescence to photosynthesis for remote sensing applications: Mechanisms and challenges. *J. Exp. Bot.* **65**, 4065–4095 (2014).
27. D. R. Bowling *et al*., Limitations to winter and spring photosynthesis of a Rocky Mountain subalpine forest. *Agric. Meteorol.* **252**, 241–255 (2018).
28. W. W. Adams, C. R. Zarter, V. Ebbert, B. Demmig-Adams, Photoprotective strategies of overwintering evergreens. *Bioscience* **54**, 41–49 (2004).
29. A. Verhoeven, Sustained energy dissipation in winter evergreens. *New Phytol.* **201**, 57–65 (2014).
30. P. Jahns, A. R. Holzwarth, The role of the xanthophyll cycle and of lutein in photoprotection of photosystem II. *Biochim. Biophys. Acta* **1817**, 182–193 (2012).
31. Sun Y *et al*., OCO-2 advances photosynthesis observation from space via solar-induced chlorophyll fluorescence. *Science* **358**, eaam5747 (2017).
32. M. Verma *et al*., Effect of environmental conditions on the relationship between solar-induced fluorescence and gross primary productivity at an OzFlux grassland site. *J. Geophys. Res. Biogeosci.* **122**, 716–733 (2017).
33. L. Guanter *et al*., Retrieval and global assessment of terrestrial chlorophyll fluorescence from GOSAT space measurements. *Remote Sens. Environ.* **121**, 236–251 (2012).
34. T. S. Magney *et al*., Connecting active to passive fluorescence with photosynthesis: A method for evaluating remote sensing measurements of Chl fluorescence. *New Phytol.* **215**, 1594–1608 (2017).
35. Y. Goulas *et al*., Gross primary production of a wheat canopy relates stronger to far red than to red solar-induced chlorophyll fluorescence. *Remote Sens.* **9**, 97 (2017).
36. L. Liu, L. Guan, X. Liu, Directly estimating diurnal changes in GPP for C3 and C4 crops using far-red sun-induced chlorophyll fluorescence. *Agric. Meteorol.* **232**, 1–9 (2017).
37. A. Damm *et al*., Impact of varying irradiance on vegetation indices and chlorophyll fluorescence derived from spectroscopy data. *Remote Sens. Environ.* **156**, 202–215 (2015).
38. S. Du, L. Liu, X. Liu, J. Hu, Response of canopy solar-induced chlorophyll fluorescence to the absorbed photosynthetically active radiation absorbed by chlorophyll. *Remote Sens.* **9**, 911 (2017).
39. K. Yang *et al*., Sun-induced chlorophyll fluorescence is more strongly related to absorbed light than to photosynthesis at half-hourly resolution in a rice paddy. *Remote Sens. Environ.* **216**, 658–673 (2018).
40. G. Badgley, C. B. Field, J. A. Berry, Canopy near-infrared reflectance and terrestrial photosynthesis. *Sci. Adv.* **3**, e1602244 (2017).
41. G. Miao *et al*., Sun-induced chlorophyll fluorescence, photosynthesis, and light use efficiency of a soybean field from seasonally continuous measurements. *J. Geophys. Res. Biogeosci.* **123**, 610–623 (2018).
42. C. van der Tol, J. A. Berry, P. Campbell, U. Rascher, Models of fluorescence and photosynthesis for interpreting measurements of solar-induced chlorophyll fluorescence. *J. Geophys. Res. Biogeosci.* **119**, 2312–2327 (2014).
43. K. Grossmann *et al*., PhotoSpec: A new instrument to measure spatially distributed red and far-red solar induced chlorophyll fluorescence. *Remote Sens. Environ.* **216**, 311–327 (2018)
44. J. Hu, D. Moore, S. Burns, R. Monson, Longer growing seasons lead to less carbon sequestration by a subalpine forest. *Glob. Chang. Biol.* **16**, 771–783 (2010).
45. W. J. Sacks, D. S. Schimel, R. K. Monson, B. H. Braswell, Model-data synthesis of diurnal and seasonal CO2 fluxes at Niwot Ridge, Colorado. *Glob. Chang. Biol.* **12**, 240–259 (2006).
46. W. W. Adams, B. Demmig-Adams, B. A. Logan, D. H. Barker, C. B. Osmond, Rapid changes in xanthophyll cycle-dependent energy dissipation and photosystem II efficiency in two vines, Stephania japonica and Smilax australis, growing in the understory of an open Eucalyptus forest. *Plant Cell Environ.* **22**, 125–136 (1999).
47. P. Yang, C. van der Tol, Linking canopy scattering of far-red sun-induced chlorophyll fluorescence with reflectance. *Remote Sens. Environ.* **209**, 456–467 (2018).
48. Y. Sun *et al*., Overview of solar-induced chlorophyll fluorescence (SIF) from the orbiting carbon observatory-2: Retrieval, cross-mission comparison, and global monitoring for GPP. *Remote Sens. Environ.* **209**, 808–823 (2018).
49. A. Porcar-Castell, A high-resolution portrait of the annual dynamics of photochemical and non-photochemical quenching in needles of Pinus sylvestris. *Physiol. Plant.* **143**, 139–153 (2011).
50. C. Buschmann, Variability and application of the chlorophyll fluorescence emission ratio red/far-red of leaves. *Photosynth. Res.* **92**, 261–271 (2007).
51. T. S. Magney *et al*., Disentangling controls on the spectral shape of chlorophyll fluorescence: Implications for remote sensing of photosynthesis. *J. Geophys. Res. Biogeosci*. Forthcoming 2019 May. doi:10.1029/2019JG005029.
52. R. K. Monson *et al*., Climatic influences on net ecosystem CO2 exchange during the transition from wintertime carbon source to springtime carbon sink in a high-elevation, subalpine forest. *Oecologia* **146**, 130–147 (2005).
53. L. P. Albert, T. F. Keenan, S. P. Burns, T. E. Huxman, R. K. Monson, Climate controls over ecosystem metabolism: Insights from a fifteen-year inductive artificial neural network synthesis for a subalpine forest. *Oecologia* **184**, 25–41 (2017).
54. R. Esteban *et al*., Internal and external factors affecting photosynthetic pigment composition in plants: A meta-analytical approach. *New Phytol.* **206**, 268–280 (2015).
55. I. Ensminger *et al*., Intermittent low temperatures constrain spring recovery of photosynthesis in boreal Scots pine forests. *Glob. Chang. Biol.* **10**, 995–1008 (2004).
56. C. Y. S. Wong, J. A. Gamon, Three causes of variation in the photochemical reflectance index (PRI) in evergreen conifers. *New Phytol.* **206**, 187–195 (2015).
57. A. Porcar-Castell *et al*., Physiology of the seasonal relationship between the photochemical reflectance index and photosynthetic light use efficiency. *Oecologia* **170**, 313–323 (2012).
58. J. A. Gamon *et al*., A remotely sensed pigment index reveals photosynthetic phenology in evergreen conifers. *Proc. Natl. Acad. Sci. U.S.A.* **113**, 13087–13092 (2016).
59. C. Frankenberg *et al*., Prospects for chlorophyll fluorescence remote sensing from the orbiting carbon observatory-2. *Remote Sens. Environ.* **147**, 1–12 (2014).
60. S. P. Burns, P. D. Blanken, A. A. Turnipseed, J. Hu, R. K. Monson, The influence of warm-season precipitation on the diel cycle of the surface energy balance and carbon dioxide at a Colorado subalpine forest site. *Biogeosciences* **12**, 7349–7377 (2015).
61. D. Moore, J. Hu, W. Sacks, D. Schimel, R. Monson, Estimating transpiration and the sensitivity of carbon uptake to water availability in a subalpine forest using a simple ecosystem process model informed by measured net CO2 and H2O fluxes. *Agric. Meteorol.* **148**, 1467–1477 (2008).
62. A. R. Desai *et al*., Seasonal pattern of regional carbon balance in the central Rocky Mountains from surface and airborne measurements. *J. Geophys. Res. Biogeosci.* **116**, 1–17 (2011).
63. P. Blanken, R. K. Monson, S. P. Burns, D. R. Bowling, A. A. Turnipseed, Data and information for the AmeriFlux US-NR1 Niwot Ridge subalpine forest (LTER NWT1) site. *AmeriFlux Manag. Proj.*10.17190/AMF/1246088.
64. R. K. Monson *et al*., Carbon sequestration in a high-elevation, subalpine forest. *Glob. Chang. Biol.* **8**, 459–478 (2002).
65. J. A. Plascyk, F. C. Gabriel, The Fraunhofer line discriminator MKII an airborne instrument for precise and standardized ecological luminescence measurement. *I.E.E.E. Trans. Instrum. Meas.* **24**, 306–313 (1975).
66. G. A. Carter, A. F. Theisen, R. J. Mitchell, Chlorophyll fluorescence measured using the Fraunhofer line-depth principle and relationship to photosynthetic rate in the field. *Plant Cell Environ.* **13**, 79–83 (1990).
67. J. Fraunhofer, Bestimmung des Brechungs- und des Farbenzerstreungs-Vermögens verschiedener Glasarten, in Bezug auf die Vervollkommnung achromatischer Fernröhre. *Ann. Phys.* **56**, 264–313 (1817).
68. N. R. Baker, Chlorophyll fluorescence: A probe of photosynthesis in vivo. *Annu. Rev. Plant Biol.* **59**, 89–113 (2008).
69. T. Wutzler *et al*., Basic and extensible post-processing of eddy covariance flux data with REddyProc. *Biogeosciences* **15**, 5015–5030 (2018).
70. H. Yang *et al*., Chlorophyll fluorescence tracks seasonal variations of photosynthesis from leaf to canopy in a temperate forest. *Glob. Chang. Biol.* **23**, 2874–2886 (2017).
71. T. Magney *et al*., Canopy and needle scale fluorescence data from Niwot Ridge, Colorado 2017-2018 (Version 1.0). CaltechDATA. https://doi.org/10.22002/d1.1231. Deposited April 25, 2019.